Chemical Engineering Journal 537 (2026) 176307

Contents lists available at ScienceDirect

Chemical Engineering Journal

journal homepage: www.elsevier.com/locate/cej

Validation of kinetic parameters based on fixed-bed experiments for hydrogen reduction of iron oxides

Emiliano Salucci [a,b,*], Antonio D'Angelo [a], Vincenzo Russo [b], Henrik Grénman [a], Henrik Saxén [a]

[a] Åbo Akademi University, Henrikinkatu 2, Turku, 20500, Finland
[b] University of Naples Federico II, Via Cintia 26, Napoli, 80126, Italy

ARTICLE INFO

Keywords:
Hydrogen
Direct reduced iron
Green ironmaking
Thermal conductivity detector
Shrinking core model
Kinetic modeling

ABSTRACT

Reducing carbon dioxide emissions from industrial processes is a major objective of current scientific research. Iron and steel production through iron ore reduction is a key contributor to greenhouse gas emissions, which can be significantly lowered using green hydrogen. However, the process involves complex, multi-scale challenges, such as reaction kinetics, thermodynamic constraints, mass and energy transport, fluid and particle dynamics, solid morphology, and economic feasibility. Based on kinetic parameters determined on a simpler system, this work focusses on a validation of these kinetic results. Validation is achieved through experimental and modeling investigations of systems with increased complexity, using the kinetic parameters previously estimated. Experiments were carried out in a packed bed reactor-like setup using pure iron oxide powder under varied operating conditions. As a novelty in this field, the thermal conductivity measurements of the product gas were quantitatively correlated to the extent of reduction of the solid sample. A mathematical model of a fixed-bed reactor, incorporating a dynamic shrinking core model, was demonstrated to accurately reproduce the experimental findings. The results emphasize the reversible nature of the chemical reactions involved and highlight the critical influence of water vapor in the systems.

1. Introduction

The ecological transition has become one of the most debated topics in recent years, as data on the climate crisis and advancing desertification become increasingly alarming. For instance, the European Union has set a target of zero greenhouse gas emissions by 2050, but the achievability of this objective is highly uncertain and could be delayed in the coming years [1]. The biggest challenge is to find environmentally friendly and innovative technologies that can be seamlessly integrated into modern anthropogenic processes, from transportation to energy supply and industry. The main problem is that although alternative processes to conventional ones exist or are being theorized, they are often not economically competitive as they are based on technologies that are either too expensive or still under development, leading to immature and inefficient production compared to the established methods. This inevitably requires the interests of the various scientific and industrial sectors to be aligned toward a common goal. The challenge is particularly pressing for the steel sector, one of the most carbon-intensive industries with estimated CO_2 emissions of around 1.85 tons per ton of steel produced [2]. Combined with a 250% increase in production observed over the last 25 years to almost two billion tons annually, the situation is becoming increasingly concerning [3]. The traditional steelmaking process is based on the Blast Furnace–Basic Oxygen Furnace (BF-BOF) route, in which iron ores (mainly iron oxides) are chemically reduced at high temperatures by carbon monoxide (CO) generated in situ through the partial combustion of coke and auxiliary reductants [4]. Although this complex metallurgical process is not the only one currently in operation, it is clearly the most widely used worldwide [5]. Over the last 50 years, various alternative routes to the blast furnace have been developed to utilize natural resources other than coal [6,7]. In the processes known as Direct Reduction (DR), the carbon source is partially replaced by gas mixtures of CO and hydrogen (H_2). Typically, the reduction process is carried out in a Shaft Furnace (SF) followed by an Electric Arc Furnace (EAF), melting the solid product—direct reduced iron (DRI)—using electrical energy [8]. Industrially operated DR processes include Midrex [9] and HYL-III [10]. The main difference between these routes lies in the H_2/CO ratio of the feed gas as well as the operating temperature and pressure. In general, the HYL-III process operates with twice the H_2/CO ratio of Midrex and under higher temperature and pressure conditions. Other industrial DR

* Corresponding authro at: Åbo Akademi University, Henrikinkatu 2, Turku, 20500, Finland.
E-mail address: emiliano.salucci@abo.fi (E. Salucci).

https://doi.org/10.1016/j.cej.2026.176307
Received 18 January 2026; Received in revised form 16 March 2026; Accepted 14 April 2026
Available online 17 April 2026

processes are Circored [11] and SL/RN [12]. These systems differ from the classical DR process mainly in the type of reactor used: SL/RN uses a rotary kiln, while Circored uses a fluidized bed. They also differ with respect to the source of the reducing gas [13]. Several studies estimate that the extensive use of DR processes could lead to a significant reduction in CO_2 emissions in the long term. Specifically, emissions from the standard SF–EAF process could be reduced by half, with an overall emission of around 0.97 tons of CO_2 per ton of steel [2]. In the case of Circored, in which only hydrogen is used as a reducing agent, the estimated emissions fall even further to around 0.2 tons of CO_2 per ton of steel [14,15]. However, there is a great deal of uncertainty regarding the technological gap associated with the continuous and sustainable production of H_2. It is estimated that the amount of green hydrogen required for a complete conversion of the industry is around 70,000 m^3 STP/h per 1 million tons of steel per year [16] — a figure that is currently far from being achievable in the short term. Therefore, with the support of the scientific community and transition-friendly policies, industrial companies need to work together to improve the efficiency and continuous applicability of green electrolysis [17] or chemical loop technologies [18,19]. To facilitate this transition, some studies have suggested introducing limited amounts of H_2 into the blast furnace [20]. This raises several questions, particularly with regard to the delicate balance of reducing agents and the safety of systems not designed to use hydrogen at temperatures above 2000 °C [21]. From a chemical point of view, the reaction network does not differ significantly between hydrogen and carbon monoxide. The reduction proceeds via a series of reversible steps from hematite (Fe_2O_3) to magnetite (Fe_3O_4) and wüstite (FeO) and finally to metallic iron (Fe). It has been shown that under the same operating conditions, reduction with hydrogen is more efficient and faster than reduction with carbon monoxide [22]. However, certain phenomena require further investigation, both in kinetic and thermodynamic terms. First, the endothermic nature of hydrogen reduction must be taken into account, as it has a negative impact on the energy balance of the reactor and requires an external energy input [23]. Secondly, the morphological evolution of the solid during reduction seems to differ significantly when using H_2 compared to CO. Some authors attribute this to the higher diffusivity of hydrogen within the solid [24]. Furthermore, the effect of water vapor, especially during the fast first reduction step, should also be investigated in more detail. Subsequent reactions are strongly influenced by the driving/reducing power of the gas mixture, which may be locally saturated with water vapor. From this perspective, an additional layer of complexity arises from the thermodynamic nature of the reaction network. The phase diagrams describing the stability of the different iron oxides are calculated based on the composition of the gas mixture, which includes both the reducing and oxidizing species formed during the reaction, as well as the operating temperature. These theoretical equilibrium curves have been determined for the reduction carried out with hydrogen, with carbon monoxide, and also for mixtures containing both reducing agents.

The Baur–Glässner/Chaudron diagrams illustrate the stability regions of each solid phase as a function of gas composition and temperature, providing a valuable thermodynamic framework for interpreting the reduction behavior of iron oxides under different atmospheres [25].

The diagram shows how the Gas Oxidation Degree (GOD) varies with the operating temperature and gas composition. In the case of H_2-based reduction, the GOD, is defined as the ratio between the water vapor concentration and the sum of the H_2O and H_2 concentrations. This definition effectively represents the molar fraction of oxidant in the system. In simple terms, the diagram allows for an analysis of the reduction potential of a gas mixture based on its composition, determining the stability regions of the different iron oxides. The same observations apply to both CO-based reduction and to mixed H_2–CO atmospheres with different molar fractions. The role of the oxidant species in the reactive system is of crucial importance but is unfortunately still often underexplored in literature. This overview illustrates the considerable complexity of the reduction process, which includes kinetic and thermodynamic mechanisms, diffusion phenomena and the structural evolution of the solid. This can lead to different reaction regimes — from kinetic to diffusion control [26,27] or even mixed and varying regimes [28,29], including solid-state diffusion [30]. To better understand the kinetics of hydrogen-based iron oxide reduction, numerous studies have investigated the effects of temperature, volumetric flow rate and gas composition [31,32]. However, the results are often difficult to compare as the technical conditions and reactor configuration vary, e.g., thermogravimetric systems, fixed beds, fluidized beds and drop tube reactors [33–36]. One of the main sources of operational variability is the solid sample itself. Many studies report that the role of impurities (gangue) in commercial solids remains unclear. While they may partially influence the final morphology of the reduced iron [37], their impact on the kinetics appears to be minor [38]. Another factor is the particle size distribution, which ranges from fines, powders obtained from ground ore to pellets [39–41]. As a result, the estimation of the kinetic parameters is subject to high variability, so that hardly any uniform results can be obtained [42]. Therefore, the present study aims to validate kinetic parameters derived from experiments on the reduction of thin layers of pure hematite powder with a defined granulometry. These parameters were obtained in a previous work, where the numerical procedures and methodologies were described in detail [43]. For clarity, all essential information required to understand and reproduce the present work is fully contained within this manuscript and its supplementary materials. This estimation dataset was chosen to minimize overlapping phenomena that could influence parametric evaluation. In particular, the use of a very thin reactive bed makes it possible to neglect diffusion-related effects, prevents the compaction of fine materials at high temperatures and limits the local thermodynamic effects of water generated during the reaction [43]. However, the predictive capability of the estimated kinetic parameters under spatially varying gas compositions and significant local H_2O accumulation had not yet been assessed. As a means to increase the system complexity, hydrogen reduction in powder beds was investigated and used to validate the estimated kinetic parameters. These experiments were performed with tenfold or more sample mass under extended operating conditions. The samples were subjected to chemical-physical analyzing before, during and after reduction, which provided an evaluation of their properties and composition, giving results that supported the theoretical and modeling assumptions. The findings demonstrate that the kinetic parameters determined precisely can accurately describe the more complex system used for validation and, furthermore, provide an interesting assessment of the role of water vapor and local thermodynamics influencing the final stages of the reduction. The present study provides mechanistic insight into phenomena that may become critical in larger-scale systems, thereby supporting the development of modern hydrogen-based reactor design strategies.

2. Materials and methods

2.1. Materials

The iron oxide samples employed in the reduction experiments were commercially sourced from Sigma-Aldrich. The specific material utilized was hematite, characterized by a chemical purity exceeding 96% and particle dimensions of <5 μm. Powder materials allow to minimize mass and heat transfer phenomena, but the substantially increased bed mass in the present experiments raises new relevant questions concerning the reduction process related to hydrogen starvation and the thermodynamic effect of water in the system. As for the gas phase, high-purity ($>$ 99.99%) hydrogen was employed as the sole reducing agent, while argon ($>$ 99.99%) served as an inert carrier. Both gases were supplied by the company Woikoski Oy, with purities sufficiently high to ensure that no side reactions or impurities would interfere with the experimental results.

2.2. Chemical and physical characterization

The specific surface area was calculated by means of the Brunauer-Emmett-Teller method. The morphological characteristics and surface structure of the samples were further examined using scanning electron microscopy (SEM). Micrographs were acquired with a NovaNanoSEM instrument, equipped with a through-the-lens detector, providing high-resolution imaging of the sample topography and compositional contrast. The thickness of the solid bed deposited during the experiment was estimated by analyzing photographs captured with a digital single-lens reflex camera (Canon EOS600D). The images were processed using specialized image analysis software, which enabled precise dimensional evaluation based on calibrated reference markers. Granulometric distribution of the solids samples was evaluated using light scattering technique (LS) through a Malvern Panalytical MASTERSIZER 3000. The monitoring of the transient chemical species through XRD analysis and of other solids proprieties during the reduction process is analyzed in detail in D'Angelo et al. works [39,40].

2.3. Reactor fluid dynamic

To achieve an accurate characterization of the reactor, residence time distribution (RTD) and axial dispersion effects were evaluated. Under standard conditions ($T = 600$ °C, $Q = 20$ mL/min), the mean residence time (τ) of the elements of fluid (i.e., H_2 in Ar) was evaluated to be 3.68 min. The axial Peclet number (Pe), expressing the ratio between convective and diffusive transport, was derived from pulse-response experiments and fitted using an unsteady-state mass balance with open–open boundary conditions. An example of model fitting is shown in Supplementary materials (cf., Fig. S1) displaying the residence time distribution function (i.e., $E(t)$ density function) over the dimensionless time θ.

Values of $Pe \approx 12$ were consistently obtained for all tested flow rates, and operating temperature, indicating deviation from ideal plug flow and the necessity of developing a model that accounts for axial dispersion phenomena.

2.4. Experimental setup

The reduction tests were carried out under various experimental conditions using an Autochem system designed primarily for chemisorption studies. A key component of the system is the thermal conductivity detector (TCD), which allows for rapid real-time monitoring of the gaseous effluents with high temporal resolution. Operating on the principle of a Wheatstone bridge, the TCD gives a signal that reflects the difference in thermal conductivity between a reference stream—argon—and the reactive gas mixture exiting the reactor, which includes hydrogen, water vapor, and argon. Fig. 2 shows a schematic representation of the experimental apparatus at a hypothetical time $t > 0$, where the solid bed has potentially different iron oxides and iron in the different layers, as well as the single particle that may have a triple reaction front at a given time.

The reactor, made of quartz glass, consists of a straight tubular body with a length of $L \approx 0.193$ m and a radius of $R = 0.011$ m. It is placed inside a compact electric furnace for accurate temperature control. A type-K thermocouple, positioned at the axial midpoint of the fixed bed, continuously monitors the temperature. The powder sample is supported on a quartz disk (pore sizes below 10–15 μm). An additional layer of quartz wool is positioned beneath the disk to prevent particle elutriation into the outlet stream. To ensure uniform heating, the temperature was ramped up linearly at a rate of 10 °C/min. A series of isothermal experiments were then conducted to evaluate the influence of key variables—including reaction temperature (T), solid mass (m), total gas flow rate (Q), and hydrogen molar fraction (y_{H_2}) in the feed stream—on the reduction behavior of the iron oxide (See Table 1).

TCD is widely accessible in conventional gas-analysis setups and provides adequate sensitivity for detecting variations in H_2 concentration within H_2/H_2O systems, where a strong thermal conductivity contrast exists between reacting species. Its intrinsic tolerance to water vapor allows direct analysis of the gas stream produced during reduction, avoiding the need for extensive pre-treatment typically required when mass spectrometer or gas chromatography systems are exposed to significant moisture. Compared to gravimetric techniques, TCD enables continuous monitoring of the gas phase under flowing conditions and avoids potential uncertainties related to buoyancy effects or fine-particle entrainment in small-mass powder systems. These features make TCD a practical, reliable, and transferable tool for real-time kinetic monitoring in hydrogen-driven reduction studies, provided that sufficient thermal conductivity contrast exists between reacting species.

To validate the TCD-based approach for monitoring iron oxide reduction with H_2, off-gas composition was analyzed using an Agilent 990 Micro GC. Consistent trends between TCD signals and Micro GC H_2 profiles (cf., Fig. S2) confirm the method's reliability. Repeatability was assessed by performing duplicate experiments under identical operating conditions. The standard deviation in raw TCD signal remained below 1% (cf., Fig. S3), indicating high experimental reproducibility. All normalized TCD data (cf., Figs. S4 and S5) are provided in the Supplementary Material. The TCD signals are presented in normalized form to facilitate direct visual comparison across different operating conditions using a common y-axis scale. For each experiment, the corresponding

Table 1
Hematite reduction experimental conditions.

Test	T [°C]	Q_{H_2} [mL/min]	Q_{Ar} [mL/min]	Q [mL/min]	y_{H_2} [−]	m [g]
1	600	4	8	12	0.33	0.1017
2	800	4	8	12	0.33	0.1140
3	1000	4	8	12	0.33	0.1011
4*	600	4	24	28	0.14	0.1005
5	800	4	24	28	0.14	0.1070
6	1000	4	24	28	0.14	0.1012
7**	600	3	17	20	0.15	0.1070
8**	600	5	15	20	0.25	0.1101
9**,***	600	4	16	20	0.20	0.1105
10	600	4	16	20	0.20	0.1483
11	600	4	16	20	0.20	0.2192
12	600	4	16	20	0.20	0.3200
13	800	4	16	20	0.20	0.1040
14	800	4	16	20	0.20	0.2000
15*	600	2	26	28	0.071	0.1002
16***	600	5	19	24	0.21	0.1071
17*,***	600	6	22	28	0.21	0.1083

*,**,*** Further comparisons between experimental tests.

maximum detector signal (in mV) is reported in the Supplementary Material (cf., Table S3). Multiplication of this value by the normalized profile allows reconstruction of the original unprocessed TCD signal.

2.4.1. Mathematical and physical interpretation of TCD signals

The analysis of the thermal conductivity signal is inherently complex due to the combined effects of the gas phase properties and the structural characteristics of the detection system (i.e., the Wheatstone bridge). The data analysis method developed to improve the interpretation of the reduction process leads to an important intermediate step in the analysis: establishing a robust correlation between the original thermal conductivity signal and the extent of solid phase conversion in the heterogeneous gas–solid reactions [43]. The procedure briefly outlined in the Appendix, involves the calculation of the accumulated hydrogen consumption and the interpretation of this with respect to the solid reduction degree. Furthermore, the presence of dead volume and axial dispersion effects in the initial part of the experiments required a correction of the signal, which was obtained by comparison with the results of the blank signal, i.e., an experiment without a solid sample. By this procedure, the dynamic effect of the introduction of the hydrogen gas in the feed flow can be appropriately considered. All normalized TCD datasets together with the corresponding calculated reduction degree profiles are provided in the Supplementary Material (Figs. S4 and S5). In addition, Figs. S6 and S7 report the blank signals employed for baseline subtraction, completing the information required to reproduce the full data processing procedure.

2.5. Mathematical model

The mathematical model facilitates a more detailed analysis of the interparticle gas composition of the solid bed, considering not only the kinetic and fluid dynamics, but also the thermodynamics of the reduction reactions, which strongly influences some phases of the process. The model applies to a granular mass balance, which takes into account the particle size distribution in the solid phase, as well as a more realistic representation of the progression of the reaction front. At its core, the model couples a traditional axial dispersion formulation with a time-dependent dynamic shrinking core model (SCM) enhanced by a product layer concept. At each time increment, the state of solids is reassessed, and the model dynamically selects the governing equations based on the number of active reaction fronts present. This strategy ensures the inclusion of a broad spectrum of transport and reaction mechanisms, including chemical kinetics, thermodynamic equilibrium, and mass transfer phenomena — both internal and external. Reactions are constrained to occur at the interface between the unreacted core and the reacted shell; as the core shrinks, the reaction surface area correspondingly decreases. In the proposed mechanism, a maximum of three concurrent reaction fronts can be active, depending on the oxide species and their extent of conversion. This kinetic model represents an advanced version of an earlier framework by the research group [44] and was used to estimate the kinetic parameters of the three reduction [43]. It is presented here in a more compact way, highlighting the main differences.

2.5.1. Solid mass balance

The model expresses the temporal t and spatial evolution of each iron oxide's molar content along the axial coordinate z_2 of the bed. The initial oxygen molar content n_0 is calculated based on the mass and molar weight (M) of the starting oxide (e.g., $n_0 = 3m/M$). The solid side mass balance describes the dynamic of the degree of conversion X_j using the ordinary differential equation

$$\frac{\partial X_j(t,z_2)}{\partial t} = (1-\varepsilon)\frac{r_j(t,z_2)}{n_0 \cdot a_j} \tag{1}$$

where the term a_j represents the fractional oxygen content depending on the oxide species. The local reduction rate r_j for each oxide is formulated as

$$r_j(tz_2) = \sum\nolimits_{n=1}^{N} x_n \cdot \frac{P}{R_g T}\frac{3}{r_n^0}\frac{1}{A_j\left(t,z_2,r_n^0\right)\big|_f}\cdot\left(\frac{N_j\left(t,z_2,r_n^0\right)\big|_f}{W\left(t,z_2,r_n^0\right)\big|_f} - y_{\mathrm{H_2}\,j,\mathrm{eq}}(tz_2)\right) \tag{2}$$

Here, R_g is the universal gas constant, P is the pressure, and $y_{\mathrm{H_2}\,j,\mathrm{eq}}$ is the equilibrium hydrogen mole fraction for reaction j. The equilibrium mole fraction $y_{\mathrm{H_2}\,j,\mathrm{eq}}$ is derived based on local gas composition ($y_{i,j}$) and the reaction-specific equilibrium constant K_j

$$y_{\mathrm{H_2}\,j,\mathrm{eq}}(t,z_2) = \frac{1}{1+K_j}\cdot\left(y_{\mathrm{H_2}\,j}(t,z_2) + y_{\mathrm{H_2O}\,j}\left(t,z_2\right)\right) \tag{3}$$

The equilibrium constants of each reactive step were calculated through the expressions

$$K_j = \exp\left(-\frac{\Delta G_j^{\circ}}{R_g T}\right) \tag{4}$$

$$\Delta G_j^{\circ} = g_{1j}\cdot T^2 + g_{2j}\cdot T + g_{3j} \tag{5}$$

where ΔG_j is the Gibbs free energy in J/mol while $g_{g,j}$ are parameters taken from thermodynamic datasets [45]. These parameters for each reaction j are reported in the Supplementary Material in Table S2.

The global reduction rate is then aggregated over all particle size classes by weighing each rate by the respective initial radius r_n^0 and weight fraction x_n, thus capturing the influence of particle size distribution on the overall conversion. The parameters A_j, N_j and W that are the kinetic resistance, the effective reduction rate, and the total resistance, respectively, are central to the dynamic selection of the governing equations. The degree of conversion X_j helps determine the number of active reaction fronts in each layer. At each simulation time of the mathematical model, the composition of the solid bed is queried layer by layer by determining the number of active reaction fronts, which can vary from 3 to 0 at the end of the reduction. The analytical equations describing the multi-front reductive processes are complex to derive [46], but easy to implement due to their mathematical nature. For this reason, the terms N_j and W evolve dynamically as the number of available reactions varies using f, which orchestrates these transitions.

$$\text{if}\begin{cases} X_1(t,z_2) = 0 \\ X_1(t,z_2) < 1 \wedge X_2(t,z_2) = 0 \\ X_1(t,z_2) < 1 \wedge X_2(t,z_2) < 1 \wedge < 0\, X_3(t,z_2) < 1 \\ X_1(t,z_2) = 1 \wedge X_2(t,z_2) < 1 \wedge X_3(t,z_2) < 1 \\ X_1(t,z_2) = 1 \wedge X_2(t,z_2) = 1 \wedge X_3(t,z_2) < 1 \\ X_1(t,z_2) = 1 \wedge X_2(t,z_2) = 1 \wedge X_3(t,z_2) = 1 \end{cases} \quad f = 1 \quad j = 1$$

$$f = 2 \quad j = 1,2$$

$$f = 3 \quad j = 1,2,3$$

$$f = 2 \quad j = 2,3$$

$$f = 1 \quad j = 3$$

$$f = 0 \tag{6}$$

Generally, N_j and W are defined starting from the kinetic resistance (A_j), the intraparticle diffusion resistance and external diffusion resistance. The analytical expressions for these terms are reported in detail in a previous work [44]. As an example, A_j is defined as

$$A_j(t,z_2)\big|_f = \frac{1}{\left(1-X_j(t,z_2)\right)^{\frac{2}{3}}\cdot k_j}\cdot\frac{1}{\left(1+\frac{1}{K_j}\right)} \tag{7}$$

where k_j is the kinetic constant. The kinetic parameters were determined

from reduction data of thin layers of pure hematite using a similar experimental and modeling approach to that described in this work. These parameters were used by means of the linearized Arrhenius equation (cf., Supplementary Material, Table S1, Fig. S8). The thermodynamic parameters were extracted from known theoretical expressions, underlying the phase diagram involving exclusively H_2-based reduction shown in Fig. 1.

2.5.2. Gas mass balance

The gas phase dynamics account for the temporal changes in the concentrations of reducing and oxidizing species. The reactor is divided into two zones — a non-reactive zone ($l = 1$) and a reactive fixed-bed region ($l = 2$) — each characterized by dimensionless coordinates z_1 and z_2, respectively.

$$\frac{\partial c_i(t,z_l)}{\partial t} = \begin{cases} -\frac{u}{L-h}\cdot\frac{\partial c_i(t,z_1)}{\partial z_1} + \frac{D_z}{(L-h)^2}\cdot\frac{\partial^2 c_i(t,z_1)}{\partial {z_1}^2} & \text{for } l=1 \\ -\frac{u}{h}\cdot\frac{\partial c_i(t,z_2)}{\partial z_2} + \frac{\partial^2 c_i(t,z_2)}{\partial {z_2}^2} + (1-\varepsilon)\cdot\sum_{j|_f}^{3}\nu_{i,j}\cdot r_j(t,z_2) & \text{for } l=2 \end{cases} \tag{8}$$

In the model equations, c_i denotes the concentration of gas species i (H_2 or H_2O), while ν_{ij} are the stoichiometric coefficients associated with reaction j. The key hydrodynamic parameters include bed height h, superficial gas velocity u, and axial dispersion coefficient D_z. The initial porosity ε of the bed was measured through physisorption techniques. Boundary conditions are specified at the reactor inlet ($z_1 = 0$), the interface between zones ($z_1 = 1$, $z_2 = 0$), and the outlet ($z_2 = 1$).

$$c_i(t,z_1)\,|_{z_1=0} = c_{i,\text{in}} \qquad \left.\frac{\partial c_i(t,z_1)}{\partial z_1}\right|_{z_1=1} = 0 \tag{9}$$

$$c_i(t,z_2)\,|_{z_2=0} = c_i(t,z_1)\,|_{z_1=1} \qquad \left.\frac{\partial c_i(t,z_2)}{\partial z_2}\right|_{z_2=1} = 0 \tag{10}$$

2.5.3. Numerical controls and solutions

The particle size distribution refined by LS techniques and the calculated external mass transfer coefficient (H) indicate that external diffusion limitations can be safely neglected since its average value is approximately 1000 m/s. This coefficient was determined based on the classical Sherwood (Sh), Schmidt (Sc), and Reynolds (Re) correlations

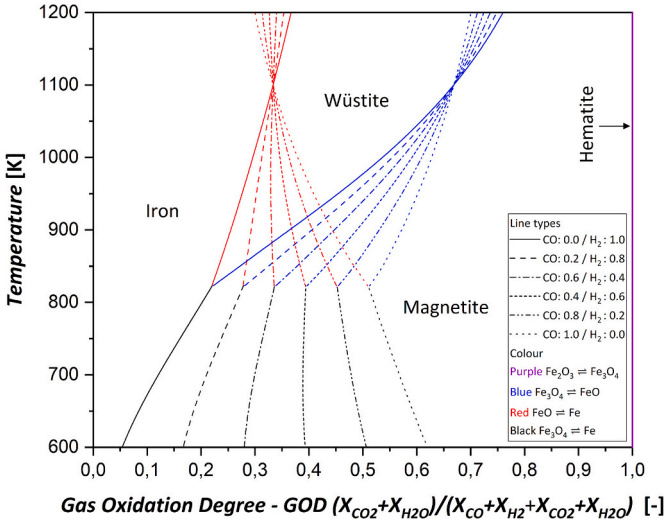

Fig. 1. Thermodynamic diagram of Baur–Glässner/Chaudron [25]. The line type indicates the composition of the H_2–CO reducing gas mixture, color denotes the equilibrium conditions of each specific reduction step.

$$H = Sh\cdot\frac{D_m}{2r_n^0} \tag{11}$$

$$Sh = 2 + 0.6Re^{1/2}Sc^{1/3} = 2 + 0.6\left(\frac{2R\cdot u\cdot\rho_g}{\mu_g}\right)^{1/2}\left(\frac{\mu_g}{\rho_g\cdot D_{mol}}\right)^{1/3} \tag{12}$$

where μ_g and ρ_g represent gas viscosity and density, respectively. The molecular diffusivity was determined according to Valipour et al. [47].

$$D_m = \frac{1\cdot10^{-7}\cdot T^{1.75}}{P\cdot\left(\sum v_i^{1/3}\right)^2}\cdot\left(\sum\frac{1}{M_i}\right)^{1/2} \tag{13}$$

where v_i is the diffusion volumes of the gas species involved. These parameters are derived from empirical equations obtained via CHEMCAD [48].

The analysis of the thermal gradients within the particles was assessed using the Mears criterion. The temperature difference between the particle surface and its center was calculated to be −0.65 K, 1.61 K, and 1.23 K for the three reduction steps, respectively. Axial temperature deviations are expected to be largest near the bed inlet, where the reaction driving force is highest, and to decrease along the bed due to hydrogen consumption and water formation. Owing to the limited bed diameter and low heat generation rate, radial temperature gradients are estimated to be below 1 K throughout the bed. These results indicate that the energy balance for the reduction of fine iron oxide beds with hydrogen can be safely neglected, as the internal temperature gradients are minimal [44]. The model was implemented in Matlab 2024a. The spatial discretization of the partial differential equations was performed with the finite difference method, using a backward differentiation scheme for first-order derivatives and a central differentiation scheme for second-order derivatives. Each axial coordinate of the reactor domain was discretized into 20 uniformly distributed nodes, and the resulting ordinary differential equations were integrated over time using the ode15s solver. A comprehensive summary of the model parameters is provided in Supplementary Materials (cf. Table S1 and Table S2).

3. Results

3.1. Materials morphology and characterization

The evolution of the chemical composition of the samples over time was examined in detail in D'Angelo et al. work [39], as it is crucial to understand the fundamentals of iron oxide reduction, particularly through XRD analysis (cf., Fig. S9). These results demonstrated that the time evolution of the TCD signal curve is directly correlated with the progress of the chemical reaction. In particular, the changes in the slope of the curve correspond to the moments when the dominant solid phase involved in hydrogen consumption changes, both kinetically and thermodynamically. This confirm that the reaction performed at a temperature above 570 °C goes through all known intermediate reaction stages, starting with hematite, then magnetite, wüstite and finally iron. To the end of analyzing chemical composition and solid transient proprieties, reduction process was carried out several times in the same operating conditions by interrupting the reduction of 0.3 g hematite bed at different time intervals. The operating condition used was 600 °C, a hydrogen molar fraction of 0.2 and a total gas flow rate of 20 mL/min. The resulting solid samples were subjected to various analyses, including SEM and nitrogen physisorption. The SEM analysis provides significant morphological and topographical information about the starting material and the samples under the reduction process. The normalized thermal conductivity signal and the results of the SEM analysis are shown in Fig. 3.

The SEM images provide important information, especially about the morphological evolution of the solid phases. Although pure hematite powder tends to agglomerate, the classical rhombohedral structure

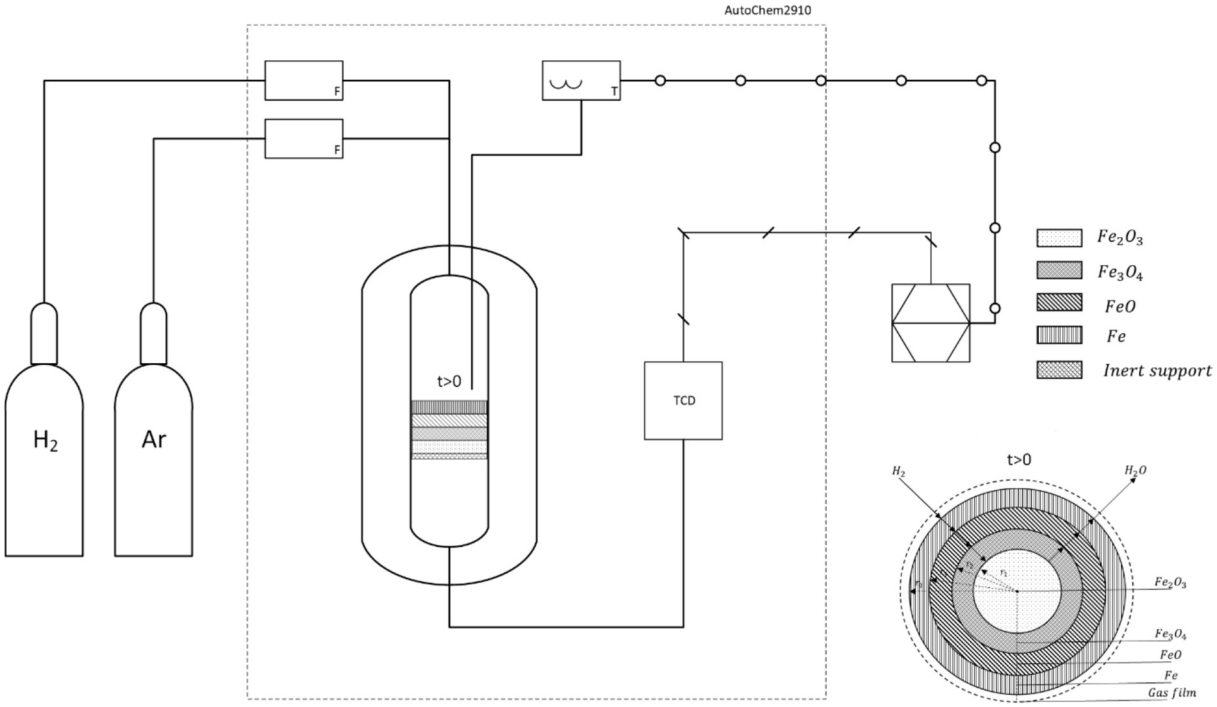

Fig. 2. Schematic of the fixed-bed experimental setup at a hypothetical time $t > 0$.

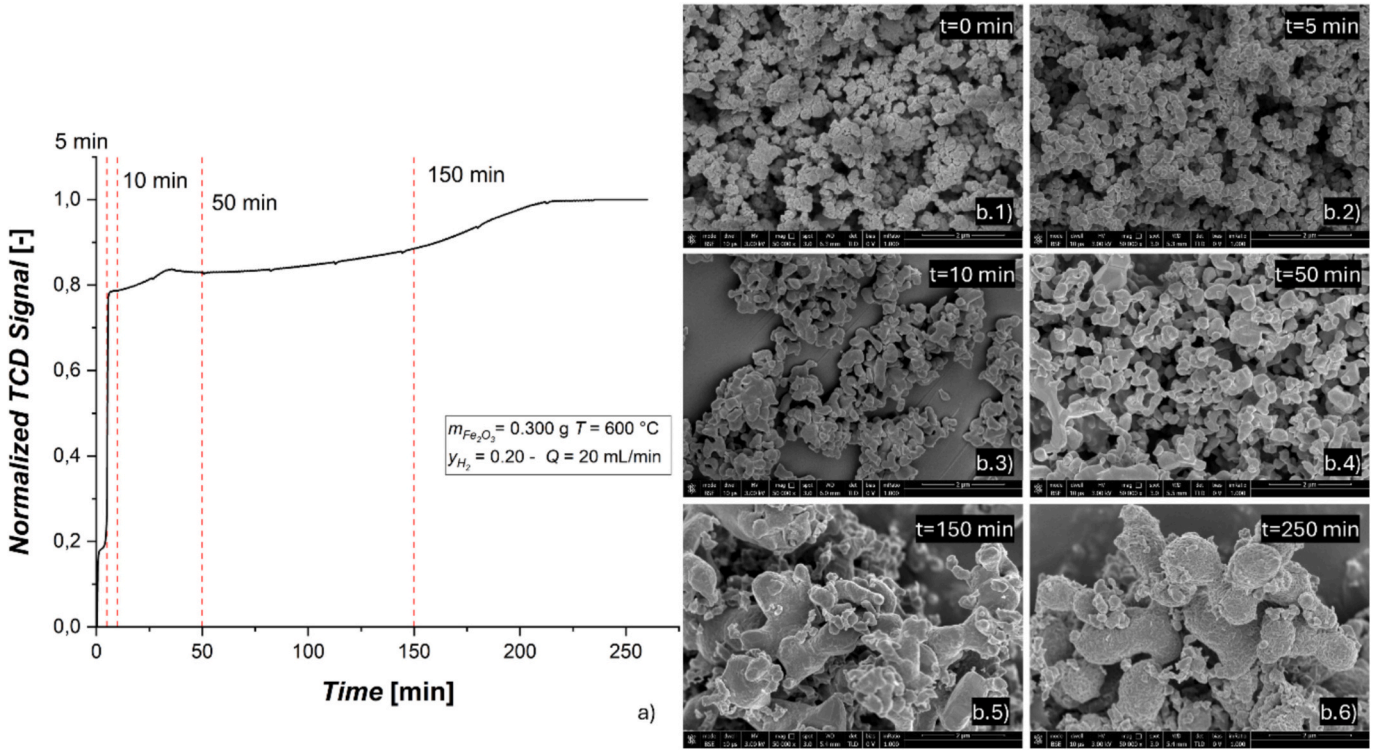

Fig. 3. a) Normalized TCD signal with stop test, b) SEM images of samples collected at different times. Experimental conditions: $m_{Fe_2O_3} = 0.300$ g, $T = 600^{\circ}$C, $y_{H_2} = 0.20$, $Q = 20$ mL/min.

remains recognizable (Fig. 6b.1). As the reaction progresses — from hematite to magnetite after 5 min or 10 min (Figs. 3b.2 and 3b.3) some coalescence of the iron oxide particles can be observed. At this stage, Fe_3O_4 is the predominant species that has formed rapidly. This phenomenon becomes evident with time, along with the disappearance of Fe_2O_3 and the presence of FeO and Fe after 50 min (Fig. 3b.4). After 150 min of reaction, increasing the magnitude in order to get more information, a clear coalescence of the particles can be seen (Fig. 3b.5). Numerous studies have reported that such coalescence can lead to the formation of dense outer iron layers that hinder the penetration of the

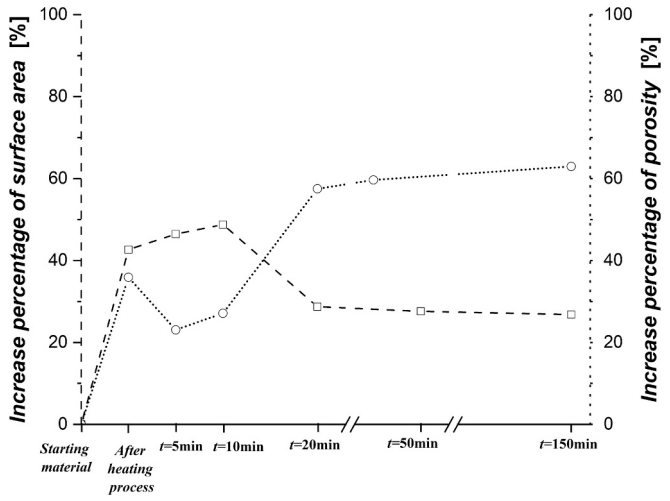

Fig. 4. Percentage change in surface area (dash line and dash y-axis) and porosity (dot line and dot y-axis) of the hematite bed samples over time.

reducing gas, resulting in incomplete reduction governed by a steady-state diffusion regime [16,49,50]. The last SEM image, Fig. 3b.6, shows the fully reduced iron after 250 min. XRD analysis of this sample confirms the exclusive presence of metallic iron, with no detectable intermediates. This morphological analysis highlights that the particle size, although the distribution may change during the reduction process, always results in dimensions comparable to the initial ones of the powder. Moreover, to determine the evolution of the size distribution of the samples over time, a light scattering technique must be used. A comparison between the particle-size distributions of the starting material and the reduced iron is reported in the Supplementary Materials (cf., Fig. S10). These results show that the occurrence of particle coalescence is present but negligible. This is evidenced by the minimal broadening of the particle-size distribution curves of the reduced iron compared to the pure hematite, as well as by the nearly identical Sauter mean diameters calculated over the entire distribution (difference of $0.22{\cdot}10^{-6}$ m). For these reasons, it was assumed that the initial particle size distribution was maintained throughout the reduction process. This assumption was also confirmed by the ability of the model to accurately describe the entire experimental data set using the initial size distribution (c.f. Results section). The specific surface area and porosity were analyzed using nitrogen physisorption and calculated using the BET method. The relative evolution of these two properties over time is shown in Fig. 4. Selected measurements were performed in duplicate to assess reproducibility. The observed variability remained within 1–2% for both porosity and specific surface area. Given this limited deviation and the substantially larger structural trends observed during reduction, additional replicates were not performed for all time points.

These results show that thermal activation of the solid occurs during the initial heating ramp of 10 °C/min and both surface area and porosity increase. At this point, a porosity of 0.1 and a surface area of about 7 m^2/g was measured. As soon as the reduction starts, opposing trends can be observed for both properties: the surface area first increases and then decreases within the first 10 min, while the porosity initially decreases slightly before increasing again. This behavior can be explained by an initial phase of rapid reduction of Fe_2O_3 to Fe_3O_4, which is accompanied by oxygen removal: the reaction creates new vacancies, which leads to an increase in surface area. The initial reduction in porosity is likely due to sintering. As the reaction progresses, new voids continue to form, but at lower reaction rates. The porosity increases while the surface area decreases due to coalescence of the particles. It is notable that the changes in both properties remain limited compared to the changes during the initial thermal activation. Starting from the initial values at $t = 0$ min (i.e., after heating process), the porosity increases overall by about 20% (from $\varepsilon = 0.1$ to $\varepsilon = 0.12$) while the surface area decreases by about 25%. These variations do not significantly affect the predicted behavior under the investigated conditions. Therefore, structural parameters were assumed constant in the present modeling framework. Specifically, the bed porosity was set its initial value, $\varepsilon = 0.1$.

3.2. Validation study

The present study on the reduction of iron oxide powder beds was carried out under different operating parameters to evaluate the influence of the fixed-bed height. The main focus is to assess the predictive capability of previously determined kinetic parameters [43] under more complex and industrially relevant conditions. No parameter fitting was performed using the experimental data presented herein; instead, the independently estimated kinetic parameters were applied unchanged to evaluate the model performance against a new and more demanding dataset. The experimental data were compared with the findings of the mathematical model that incorporates the kinetic parameters for each reduction step estimated. The reduction experiments included an extensive set of experimental conditions designed to stress both the experimental setup and the robustness of the mathematical model. The aim was to evaluate the kinetic behavior and especially the thermodynamic constraints imposed by water vapor in the bed. A preliminary theoretical analysis [44] showed that the lower layers of the bed differ significantly from the upper layers in the case of a significant bed height.

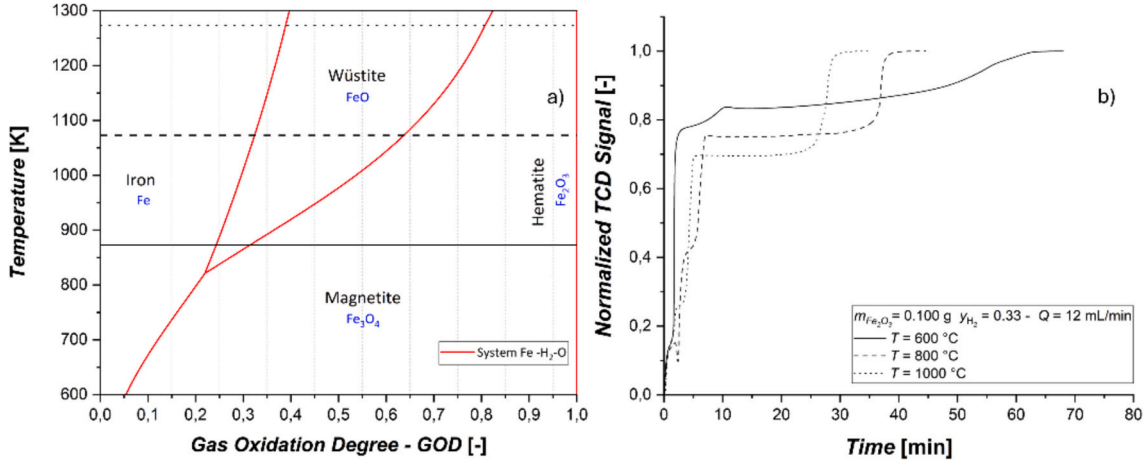

Fig. 5. a) Baur-Glässner Diagram with operating temperatures; b) Temperature effect on the normalized TCD signal for Fe_2O_3 bed reduction. Experimental conditions: $m_{Fe_2O_3} = 0.010$, $y_{H_2} = 0.20, Q = 20$ mL/min. $T = 600^{\circ}$C, 800°C and 1000°C.

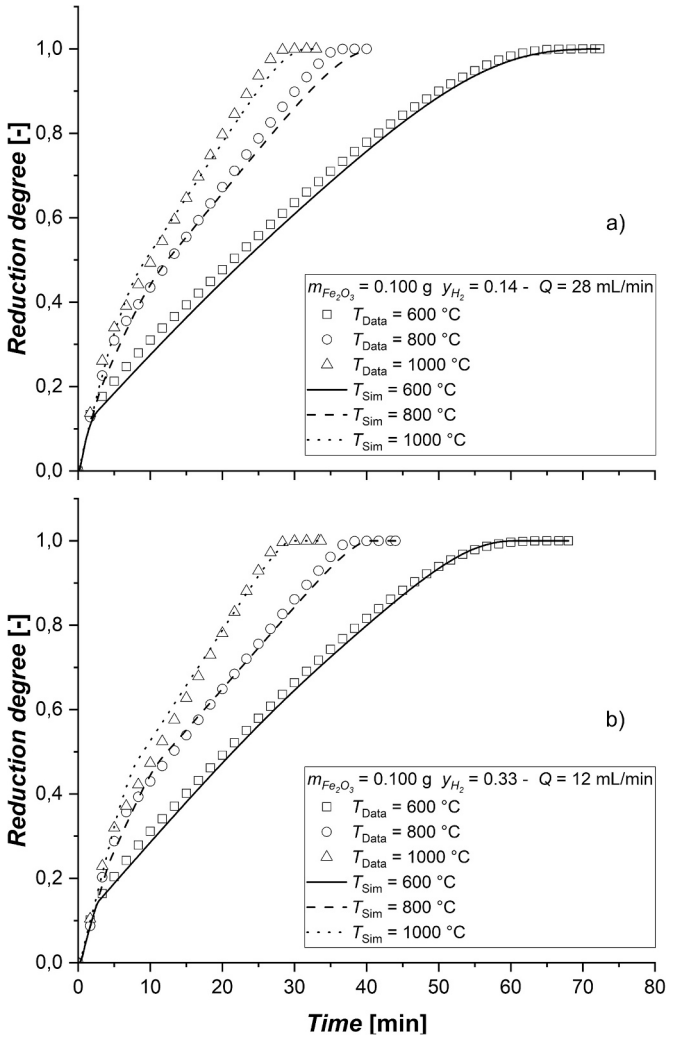

Fig. 6. Effect of temperature on Fe_2O_3 bed reduction for $m = 0.100$ g and $Q = 28$ mL/min, with a) $y_{H_2} = 0.14$ and b) $y_{H_2} = 0.33$. Experimental results are indicated by markers, simulated results by solid, dash-dotted, and dotted lines.

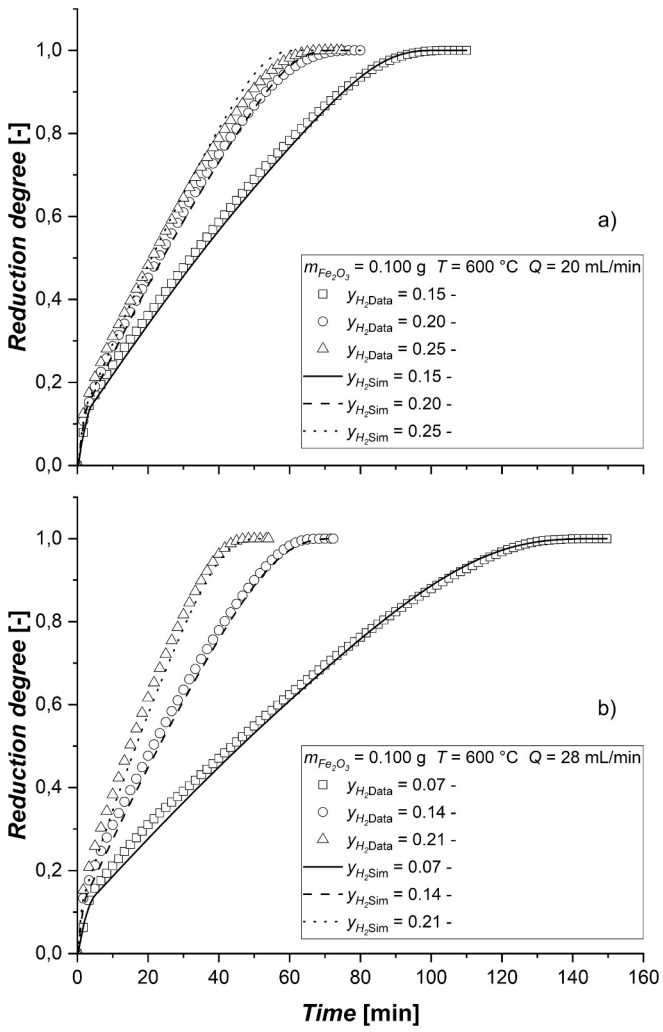

Fig. 7. Effect of hydrogen mole fraction and feed gas rate on Fe_2O_3 bed reduction for $m = 0.100$ g and $T = 600^{\circ}$C.Experimental results are indicated by markers, simulated results by solid, dash-dotted, and dotted lines.

The model revealed that as the upper layers are exposed to fresh H_2, they react rapidly under the strong driving force, while the lower layers are subjected to water vapor generated in the upper layers. This leads to a significant slowdown in the reduction process, especially in the reactions involving magnetite and wüstite [44]. Such phenomena are critical to consider for scale-up problems, e.g., to furnaces of industrial size. In addition, the morphological evolution of the material — driven by slower reaction rates under thermodynamic constraints — can lead to structural rearrangements as the system has both time and energy to stabilize in more ordered configurations. The comparison between the experimental and modeled results, processed according to the method of integration and correction of the blank experiments (cf. Materials and methods section) confirms the ability of the model to accurately interpret the phenomena occurring during the reduction process and thus validate the kinetic parameters. This also underlines the reliability of the interpretation of the thermal conductivity signal of the outlet gas. In the reduction of hematite beds, the slope changes in the curves of the thermal conductivity signals are much more pronounced than in the thin layers [39] reduction experiments due to the enhanced phenomena in bed systems, which often make all transitions between regimes more clearly visible. Fig. 5 highlights the variability in the shape of the normalized TCD signal as a function of operating temperature.

The temperature shows a remarkable effect on the appearance of the TCD signal, and, in particular, on the slope changes. At 600°C the TCD

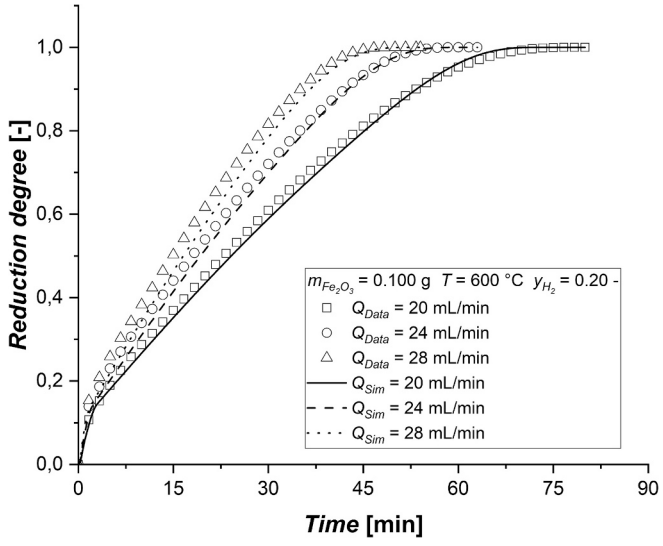

Fig. 8. Effect of feed gas rate on Fe_2O_3 bed reduction for $m = 0.100$ g, $T = 600^{\circ}$C and $y_{H_2} = 0.20$. Experimental results are indicated by markers, simulated results by solid, dash-dotted and dotted lines.

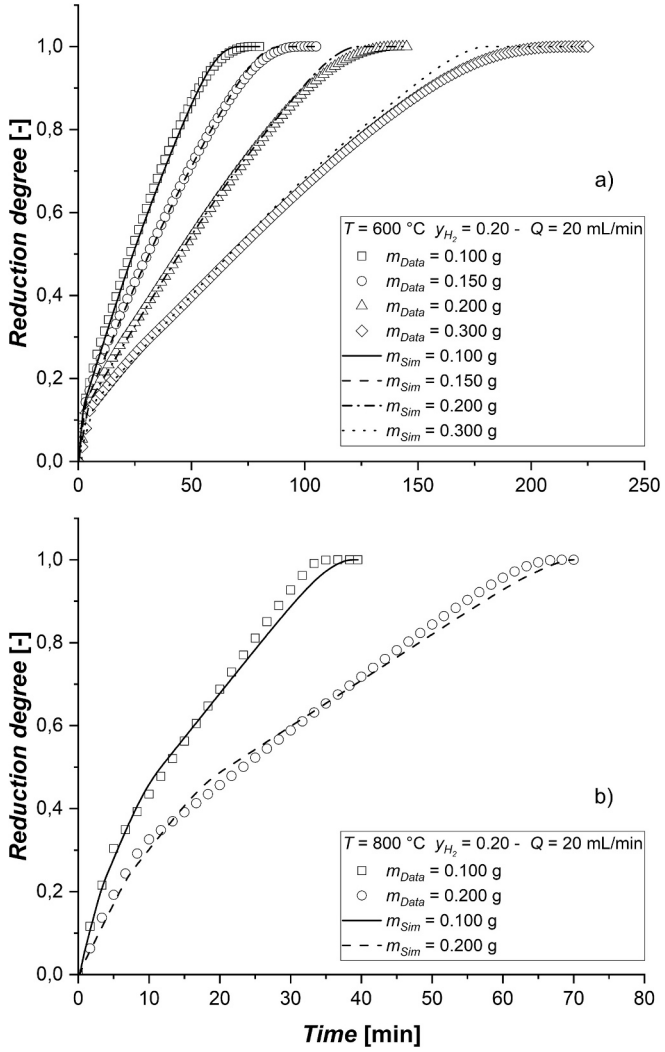

Fig. 9. Effect of solid mass on Fe_2O_3 bed reduction at a fixed gas flow rate of $Q = 0.20$ ml/min for a) $T = 600^{\circ}$C, $y_{H_2} = 0.07$, and b) $T = 800^{\circ}$C, $y_{H_2} = 0.20$. Experimental results are indicated by markers, simulated results by solid, dash-dotted, and dotted lines.

signal appears relatively smoothly, whereas at 800 °C and above the curves change significantly. In particular, the plateaus indicate that the system is not able to consume more hydrogen than reflected in the signal, implying a constraint that is due to insufficient driving force.

The Baur–Glassner diagram confirms that the stability region for metallic iron expands with increasing temperature, so that the final reduction can take place even at slightly higher water vapor content. In the normalized TCD signal, this becomes clear when comparing the signal values, as the plateau observed at 1000 °C is lower than that at 800 °C. These thermodynamic constraints are not as clearly visible in the global reduction degree, which is, however, easier to model due to its more monotonic behavior. The TCD signal and the global reduction degree are discussed in more detail in the Discussion section to complete the kinetic, modeling, and thermodynamic interpretation of the reduction process. A comparison between pure and commercial ironmaking materials has also shown that the morphological characteristics of the sample can further influence the interpretation of the TCD signal [39]. Porosity, exposed surface area and their evolution during the chemical reaction are of crucial importance when it comes to accurately describing complex experimental data sets [40]. To improve the readability of the experimental data obtained by TCD sensor and considering the high temporal resolution of the measurement, the signal was down-

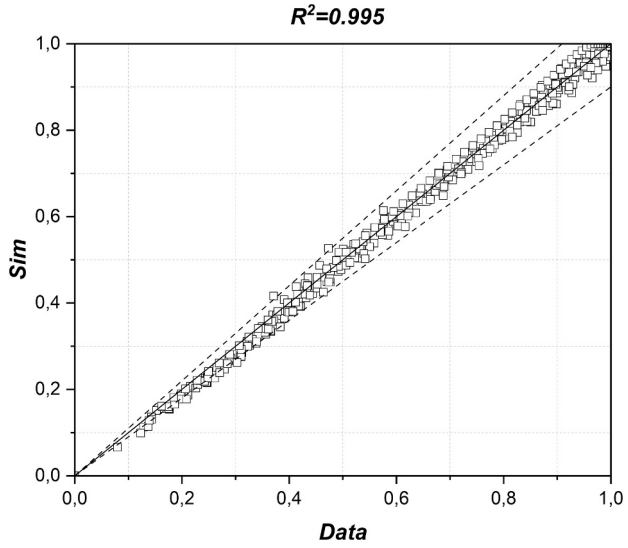

Fig. 10. Reduction degree parity plots for Fe_2O_3 bed reduction. Experiments vs. model results.

sampled to 20 s between the points.

3.2.1. *Temperature effect*

The significant influence of temperature takes on more nuanced implications when going beyond the key findings presented in thin layers experiment work [39]. In particular, in the case of powder bed, which — within certain limits — can be considered analogous to a pellet consisting of microscopic grains, high temperatures can promote not only the well-known kinetic and thermodynamic effects, but also critical morphological and structural transformations. Numerous studies have reported that sintering in the final stages of reduction can lead to solid-state diffusion regimes [51,52]. This phenomenon is often associated with the crystallographic transition of iron above 912 °C from alpha-Fe (body-centered cubic) to gamma-Fe (face-centered cubic), which is more compact and denser [42]. Such a structural change hinders the diffusion of reducing agents and increases the retention of oxidizing agents. This slows down the reduction process both from a kinetic and thermodynamic point of view. Several authors also reported about the formation of dense iron shells surrounding an unreacted FeO core — especially during the reduction of pellets [16]. However, as noted in the morphological and structural analysis section of this study, temperature does not appear to be a dominant factor in the development of the solid structure in the case of this powder bed. In particular, no pronounced late-stage deceleration indicative of a transition toward a solid-state diffusion-controlled regime was observed at 1000 °C, nor was evidence found for the formation of a compact, diffusion-limiting metallic layer under the investigated powder-bed conditions. The markers in Fig. 6 show the effect of temperature on the overall degree of reduction of pure hematite beds over time for three different temperatures (600 °C, 800 °C and 1000 °C) within the interesting range of shaft-furnace operation. Comparison between Figs. 5 and 6b illustrates how different interpretations can arise from relatively simple mathematical manipulations of the TCD signal. The most clearly recognizable change in slope corresponds to the end of hematite reduction and typically occurs at a degree of conversion of just over 0.11. This result differs from the theory due to a partial reduction of the upper magnetite layers overlapping with the first reduction step: the constant availability of fresh hydrogen and the low share of water vapor in these layers makes magnetite reduction to wüstite possible. Further insight into this behavior is provided by the mathematical model, which shows the rapid completion of the first two reductions in the upper regions of the bed. This model information is presented in the Supplementary Materials (cf.,

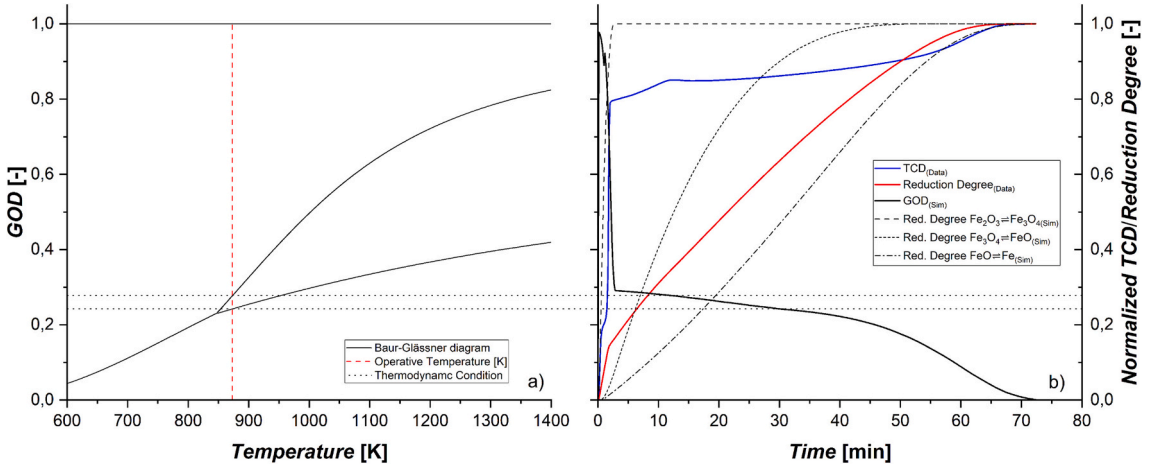

Fig. 11. Interpretation of Fe_2O_3 bed reduction experiments at 600 °C under the conditions $m = 0.100$ g, $y_{H_2} = 0.14$ and $Q = 28$ mL/min. a) thermodynamic interpretation, and b) kinetic data and simulation results.

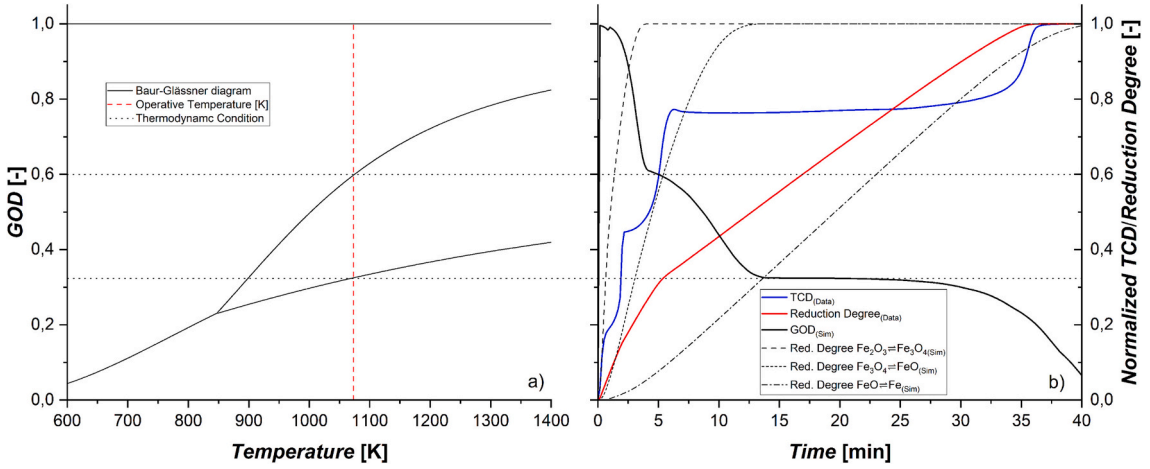

Fig. 12. Interpretation of Fe_2O_3 bed reduction experiments at 800 °C under the conditions $m = 0.100$ g, $y_{H_2} = 0.14$ and $Q = 28$ mL/min. a) thermodynamic interpretation, and b) kinetic data and simulation results.

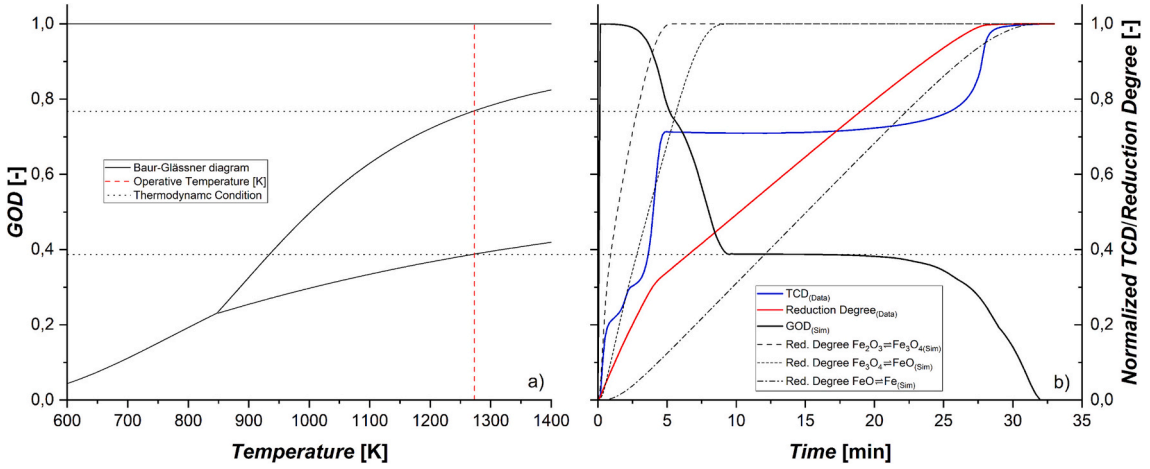

Fig. 13. Interpretation of Fe_2O_3 bed reduction experiments at 1000 °C under the conditions $m = 0.100$ g, $y_{H_2} = 0.14$ and $Q = 28$ mL/min. a) thermodynamic interpretation, and b) kinetic data and simulation results.

Fig. S11) in the form of contour plots of the composition of the solid and gas components as a function of time and space (i.e., axial coordinate of the fixed bed). The other more pronounced slope changes in the TCD signal are not as clearly reflected in the overall conversion curve, because of a continuous overlap of Fe_3O_4 and FeO reduction. For this reason, a potential slope changes at a conversion slightly above 0.3,

which corresponds to a complete and rapid end of the magnetite reduction, are rarely detectable. The phase of thermodynamic limitation is clearly visible here. The flatter the plateaus of the TCD signal, the more linear the reduction curve becomes, reflecting a constant reduction rate. The mathematical model also shows that the lower regions of the bed are exposed to high concentrations of water vapor, which is generated in the upper zones and transported downwards (cf., Fig. S11). Within certain limits, this leads to significantly different reduction times for magnetite and wüstite. The two sets of experiments shown in Fig. 6 offer valuable insights into the role of temperature. Under different operating conditions, the reduction times appear similar at 1000 °C due to the enhanced reaction rate, which makes it difficult to distinguish between the experimental cases. However, the analysis changes at lower temperatures, where differences emerge both in the overall reaction times and in the slopes of the reduction curves. This not only underscores the global importance of all operating conditions—discussed in detail in the following subsections—but also highlights the critical influence of combined kinetic and thermodynamic effects, which are primarily governed by the operating temperature. As observed by the continuous lines in Fig. 6, which represent the results of the model, it has accurately captured the behavior in the bed experiments at all three temperatures studied despite the wide operating variety.

3.2.2. Effect of gas composition

Changes in the composition of the feed gas influence the driving force of the reduction reaction. Fig. 7 shows the effects of hydrogen molar fraction on the overall degree of reduction of hematite beds over time for two different gas feed flow rates, 20 mL/min and 28 mL/min. The results indicate that an increased hydrogen concentration in the feed gas faster reactions and a decrease in the overall time to full reduction of the sample. However, the high molar ratio of H_2:Ar plays a decisive role here not only in improving the reaction kinetics, but also in influencing the thermodynamic behavior. The most obvious effect is the non-linear decrease in global reaction time. Fig. 7a shows this clearly: the reduction curves for $y_{H_2} = 0.20$ and $y_{H_2} = 0.25$ almost overlap at $Q = 20$ mL/min. This slowdown is due to the large amount of water vapor produced, which drastically decreases the driving force in the lower layers of the bed. For the larger feed gas flow rate (Fig. 7b) an increase in the feed hydrogen content has a much stronger effect, because more hydrogen is brought into the system making hydrogen starvation less severe. Note that different feed gas hydrogen concentrations were applied in the two cases to make the overall reduction time comparable. In terms of molar flow of pure hydrogen into the system, the cases in Fig. 7a represent 3.0 mL/min, 4.0 mL/min and 5.0 mL/min, while the cases in Fig. 7b represent 1.96 mL/min, 3.92 mL/min and 5.88 mL/min. Despite these differences in the conditions, the model (continuous lines) is seen to reproduce all experimental trends extremely accurately.

3.2.3. Effect of volumetric gas flow rate

As noted above, the total volumetric flow rate, Q, of feed gas plays an important role since it affects the rate of hydrogen introduced into the system and thus influences the possible starvation of the reductant in the process. Fig. 8 shows the effect of the feed gas flow rate on the overall reduction behavior at 600°C for a fixed hydrogen molar ratio, $y_{H_2} = 0.20$, in the feed gas. Increasing the flow rate clearly reduces the overall reduction time, and the change appears to vary almost linearly with the feed flow rate. It is interesting to note that this variable was the least influential one in the thin-layer experiments [39], but here it proves to be significant due to the larger bed mass. The model's results again show excellent agreement with the experimental findings for all values of Q.

3.2.4. Bed mass effect

The effect of the solid sample mass introduced into the reactor determines not only the amount of oxide to be reduced, but more importantly how the bed height affects kinetics and thermodynamics. The bed can be discretized into layers that each correspond to thin sample layer, with the main difference that the gas composition experiences changes in the consecutive layers of the bed. The deeper layers of the bed will thus encounter a gas with less hydrogen and more water vapor, imposing thermodynamic limits for the reduction reactions. This applies as long as the morphological and structural nature of the sample does not change much compared to its initial state. A temperature of 600 °C is a good choice, as it marks the entry point of the FeO stability region and serves as a practical operating temperature at which the solid properties can be assumed to be constant. Fig. 9 shows the effect of the solid mass on the reduction behavior at $T = 600^{\circ}C$ and $y_{H_2} = 0.07$ (c.f. Fig. 9a) as well as at $T = 800^{\circ}C$ and $y_{H_2} = 0.20$ (c.f. Fig. 9b). The total reduction time naturally increases with the mass of the solid sample and the relation is quite linear. At 600 °C, the reduction time increases linearly with solid mass. The mathematical model accurately describes the behavior, demonstrating that the effect of the spatial coordinate has been considered appropriately. The experiment at the higher temperature validates the model under more extreme conditions. Even though some small discrepancies can be observed, the model provides a very good fit, demonstrating its ability to capture the reduction behavior over a wide range of conditions.

4. Discussion

The analysis of the findings of reduction experiments in beds of hematite powder compared with the simulation results has confirmed and validated the ability of the mathematical model to accurately describe the key phenomena of the reduction process. The agreement between simulations and experiments must be interpreted in light of the fact that no parameter adjustment was performed for the present dataset. The model response therefore reflects the genuine predictive performance of the previously established kinetic framework [43] under conditions that significantly differ from those used for parameter estimation. The study demonstrates that adding more complexity to the experimental system — by significantly increasing the height of the fixed bed subjected to reduction — did not alter the control regimes identified during the parametric estimation using infinitesimal amount of sample [43]. This implies that the mechanisms used to describe the process remain valid and that the simplifying assumptions, such as constant bed porosity and the use of the initial size distribution, are still appropriate. A summary of validation of the model's accuracy to describe the experimental results is provided in the parity plot of Fig. 10, which holds the results from all 17 experiments presented in this paper, downsampled to 50 s between the points. The markers are well aligned along the diagonal of the diagram, which is confirmed by the high R^2 value. This comparison also reveals that the most critical stage of the modeling is the transition from Fe_3O_4 to FeO, as the last two reduction steps partially overlap. To further investigate the inter-particle dynamics, a series of simulation-based experimental case studies were carried out with the aim to isolate and analyze the most important control mechanisms under variable operating conditions, and, in particular, temperature. It is well known that not only kinetics and mass transfer, but also the thermodynamic constraints of the process change considerably with temperature. For example, below 570 °C (about 840 K, cf. Fig. 1) the reduction sequence is limited to only two reactions. Figs. 11–13 show simulated kinetic and thermodynamic details of bed reduction experiments carried out at 600 °C, 800 °C, and 1000 °C, respectively, as well as the TCD signal and the corresponding reduction degree estimated based on it.

The experimental data sets ($m = 0.100$ g, $y_{H_2} = 0.14$ and $Q = 28$ mL/min) used for this analysis were augmented in panels b by simulation results of the GOD, calculated from the composition of the outlet gas, and by average values of the solid phase reduction degrees for the three reaction steps. Panels a, in turn, show the corresponding thermodynamic Baur–Glassner diagram for each set of experimental conditions, and the furnace temperature (red dashed vertical line) as

well as the corresponding GOD values of the Fe_3O_4-FeO and FeO-Fe equilibria (horizontal dotted lines, extended into panels b).

Fig. 11 shows data for hematite reduced at 600 °C. A first notable observation is the initial peak in the GOD, which reflects the complete conversion of the available hydrogen to water vapor. This initial Fe_2O_3 reduction step is not thermodynamically limited and can be completed within a few (~ 4) minutes. This rapid reduction is reflected in a change in the slope of both the TCD signal and the calculated reduction degree. The subsequent reduction steps start more slowly due to strong thermodynamic limitations. During the transition after the complete reduction of hematite, the GOD (and thus the water content) decreases, allowing the later reactions to proceed. While only the outlet gas and average conversion values are illustrated in this analysis, it is important to note that the reactions in the upper bed layers, which are always exposed to fresh H_2, always progress faster in the later reaction steps (cf., Fig. S11). However, due to the strong thermodynamic constraints in the lower parts of the bed, their contribution to the overall conversion is initially low. In the time interval 4–10 min, a significant Fe_3O_4 consumption occurs, which leads to the stabilization of the GOD. The subsequent change in the TCD slope after 10 min correlates with the moment when about 50% of the Fe_3O_4 is converted to FeO. This marks the transition to a new predominant solid species that drives the consumption of the reductant. After 20 min, FeO begins to form in the lower bed layers ($X_3 \approx 0.3$), while the Fe_3O_4 reduction approaches completion ($X_2 > 0.7$). The last FeO-to-Fe reduction phase is the slowest and takes almost an hour to complete. This is largely due to the fact that most of the water vapor is released during this last step, reducing the driving force in the underlying bed layers. The GOD is seen to remain in the stability region of FeO for about 30 min before it drops, which eventually allows for a faster reaction rate. After about 50 min, the magnetite is completely reduced, and another 25 min are needed for the complete reduction of wüstite.

Increasing the temperature significantly enhances the reduction rate. Thermodynamically, Fig. 12 shows that the stability range of FeO expands so that it can also form in the presence of much more water vapor in the gas. The same holds true — albeit to a lesser extent — for the FeO-to-Fe step, due to the differences in the monotonicity of the equilibrium curves. Interestingly, the conversion rate of Fe_2O_3 to Fe_3O_4 is comparable to that observed at 600 °C. This is due to the higher and simultaneous H_2 consumption by Fe_2O_3 and Fe_3O_4, which has two effects: (1) more water vapor is produced, with a much broader GOD peak than before, affecting thermodynamics; (2) kinetic competition occurs, with the upper layers consuming more reductant required by the unreacted hematite in the lower layers, resulting in multi-layer competition. As a result, Fe_2O_3 and Fe_3O_4 reach complete reduction after ~4 min and ~ 12 min, respectively. These transitions are clearly visible in the experimental TCD signal, with the changes in the slope reflecting the dominant reaction stage. After Fe_3O_4 has reached a conversion of more than 80%, the GOD decreases and enters the wüstite stability region. Initially, the FeO reduction is limited by the high GOD and does not participate in the competition for hydrogen with Fe_2O_3 and Fe_3O_4. Only when the magnetite reduction approaches completion, the TCD signal stabilizes (at t = 5–6 min), followed by a drop in GOD to the thermodynamic threshold for the final FeO reduction. The water content remains high, and since FeO is the only active phase, thermodynamic limitations dominate. The practically constant TCD signal confirms that the system cannot consume more hydrogen than thermodynamically allowed. As soon as the wüstite conversion exceeds 80%, GOD drops again, and the remaining oxides are reduced.

Fig. 13, illustrating the conditions at 1000 °C, further emphasizes the observed dynamics. The multilayer competition between Fe_2O_3 and Fe_3O_4 remains, but the stability range of FeO shifts — wüstite can now be produced for GOD <0.8, which accelerates its formation. The new bottleneck is reached in the third step: GOD = 0.4 marks the thermodynamic limit of the process. A complete reduction is achieved shortly before t = 35 min.

Given the comparative results between experimental and simulated data (i.e., TCD signal and GOD), the behavior of the normalized TCD signals for hematite-bed reduction at different operating temperatures, as shown in Fig. 5b, becomes clearer. In particular, the different flat-region values correspond to different operating points of the chemical reaction along the equilibrium curve of the Baur–Glässner diagram for the wüstite–iron reaction. Each temperature thus leads to a distinct possible thermodynamic limitation for the wüstite-to-iron reaction, which determines a different outlet hydrogen fraction. Consequently, the normalized TCD signals exhibit different plateau levels, each reflecting a specific thermodynamic limitation.

This validation has highlighted the identification and analysis of fundamental aspects of iron oxide reduction under increasingly complex system conditions compared to the thin-layer experiments [39]. It is evident that in the absence of mass transfer limitations, thermodynamics plays a central role — in some stages even more prominently than intrinsic kinetics — in defining the reduction dynamics and reactor behavior. While the present study is conducted at laboratory scale, temperature remains the primary transferable operating parameter, as it simultaneously governs kinetics, equilibrium constraints, and transport phenomena. The mechanistic insight obtained here provides a consistent and structured basis for future multiscale extensions of the modeling framework, including grain-based pellet descriptions and pilot-scale reactor simulations. In this sense, the present validation constitutes a necessary intermediate step between intrinsic kinetic estimation and reactor-scale modeling.

The present modeling framework is formulated for fine powder beds under conditions where structural evolution does not introduce additional intraparticle diffusion limitations. It should be emphasized that for larger particles or industrial pellets, high-temperature reduction may involve significant structural transformations, including pore closure, crack formation, and densification phenomena, which can alter the dominant rate-controlling mechanism. In such cases, coupling of the present kinetic framework with grain-scale or intraparticle diffusion models would be required to ensure accurate predictive capability. Analogous thermodynamic limitations have also been reported in simulations of industrial-scale direct reduction processes [53]. The current study therefore defines a validated applicability range for micron-scale powder systems, establishing a clear pathway toward future multiscale model development.

5. Conclusions

The main aim of this work was to validate the kinetic parameters estimated for the reduction of pure iron oxide powders by means of experiments on thin hematite layers. The experimental system was extended to a bed of particles, where the conditions change spatially due to the effect of the reduction reactions on the gas composition. The study was not only designed to assess the accuracy of the kinetic parameters, but also to reveal possible limitations in the applicability of the kinetic model to more complex systems. A comprehensive experimental matrix was developed covering a wide range of operating conditions such as temperature, solids mass, hydrogen molar fraction, and total gas flow rate. The experiments were conducted using a PBR system, i.e., Autochem 2910 equipped with a thermal conductivity detector for gas analysis.

The main findings of this study can be summarized as follows:

- TCD signal quantitatively correlated with the solid-phase conversion degree;
- The previously determined kinetic parameters accurately describe the reduction behavior in a packed-bed system, with no change in the controlling regimes compared to the estimation conditions;
- The coupled shrinking-core and axial dispersion model successfully captures all major stages of the reduction process;

- Thermodynamic limitations arising from local water vapor accumulation (i.e., low driving force) significantly affect the reduction rate, particularly in the lower regions of the bed;
- The hematite-to-magnetite transition proceeds rapidly and is only weakly influenced by thermodynamic constraints, whereas the subsequent reduction steps are increasingly governed by local gas composition;
- The modeling framework remains robust across a wide range of temperatures, solid masses, hydrogen concentrations, and gas flow rates.

These findings support the validity of the combined experimental and model-based approach as a robust tool for analyzing fine iron oxide reduction systems within the investigated micron-scale powder-bed operating conditions. Extension to larger particles or industrial pellet-scale configurations will require explicit incorporation of intraparticle diffusion mechanisms and structural evolution effects. Additional phenomena are expected to influence the overall behavior, including intra-pellet diffusion limitations, morphological evolution such as pore closure and sintering, structural heterogeneity, and the presence of gangue minerals and binders typical of industrial materials. These factors may intensify local thermodynamic constraints and modify the effective reaction pathways compared to pure oxides. Future work should therefore focus on disentangling intrinsic kinetic effects from transport and structural phenomena in commercial materials, enabling a more comprehensive understanding of hydrogen-based industrial iron-making systems.

Notation

Abbreviations

BF	Blast Furnace
CFD	Computational Fluid Dynamic
GOD	Gas Oxidant Degree
DRI	Direct Reduction Iron
LS	Light scattering
RTD	Residence time distribution
SCM	Shrinking core model
TCD	Thermal conductivity detector

Symbols

A_j	Kinetic reaction resistance [s/m]
a_j	Proportional oxygen content parameter [−]
c_i	Concentration *i*:th gas in the reactor [mol/m^3]
$c_{i,\mathrm{in}}$	Feed *i*:th gas concentration [mol/m^3]
D_m	Molecular diffusivity coefficient [m^2/s]
D_z	Axial dispersion coefficient [m^2/s]
$E(t)$	Density function [−]
$g_{g,j}$	Gibbs energy parameter coef. ($j = 1$ [J/(mol K^2)], $j = 2$ [J/(mol K^2], $f = 3$ [J/mol])
H	External diffusion coefficient [m/s]
h	Height of the solid bed [m]
K_j	Equilibrium constant *j*:th reaction front [−]
k_j	Kinetic constant *j*:th reaction front [m/s]
L	Reactor length [m]
M_i	Molecular weight [g/mol]
m	Iron oxide initial mass [g]
N	Number of granulometric families [−]
N_j	Effective reaction SCM term ($f = 1$ [−], $f = 2$ [s^2/m^2], $f = 3$ [s^3/m^3])
n_0	Initial concentration of oxygen [mol/m^3]
P	Operating pressure [N/m^2]
Pe	Pcclet number [−]
Q	Volume flow rate [mL/min]
R_g	Universal gas constant [J/(K mol)]
Re	Reynolds number [−]
r_n^0	Iron oxide particle radius [m]
r_j	Reduction rate SCM [mol/(m^3 s)]

(*continued on next column*)

(*continued*)

Sc	Schmidt number [−]
Sh	Sherwood number [−]
T	Operating temperature [K]
t	Time [s]
u	Gas velocity [m/s]
W	Total resistance ($f = 1$ [−]) ($f = 2$ [s^2/m^2]) ($f = 3$ [s^3/m^3])
X_j	Reduction degree *j*:th reaction front [−]
x_n	Weight granulometric distribution [−]
$y_{i,j}$	Gas molar fraction *i*:th species of *j*:th reaction front [−]
$y_{\mathrm{H_2},j,\mathrm{eq}}$	Equilibrium molar fraction of H_2 of *j*:th reaction front [−]
z	Reactor axial coordinate [−]
ΔG_j°	Standard Gibbs free energy change [J/mol]
ε	Bed void degree [−]
ρ_g	Gas density [g/cm^3]
$\nu_{i,j}$	Stoichiometric matrix [−]
μ_g	Gas viscosity [Pa s]
τ	Mean resident time [min]

Subscripts

f	Number of available reaction fronts
i	Gas species
j	Reaction fronts
l	Spatial reactor domain
n	Index of granulometric family's distribution

Superscripts

0	Index of initial condition [−]

CRediT authorship contribution statement

Emiliano Salucci: Writing – original draft, Visualization, Investigation, Funding acquisition, Formal analysis, Data curation, Conceptualization. **Antonio D'Angelo:** Data curation. **Vincenzo Russo:** Writing – review & editing, Supervision, Conceptualization. **Henrik Grénman:** Writing – review & editing, Supervision, Project administration, Conceptualization. **Henrik Saxén:** Writing – review & editing, Project administration, Methodology, Funding acquisition, Conceptualization.

Declaration of competing interest

The authors declare that they have no known competing financial interests or personal relationships that could have appeared to influence the work reported in this paper.

Acknowledgement

We gratefully acknowledge financial support from the European Union within the projects *Minimisation of CO_2 emissions from the BF by hydrogen containing injectants and use of DRI/HBI during transition to new ironmaking processes until 2030* (grant agreement 101057790) and *Maximise H_2 Enrichment in Direct Reduction Shaft Furnaces* (grant agreement 101058429). Views and opinions expressed in the paper are, however, those of the authors only and do not necessarily reflect those of the European Union, so the European Union cannot be held responsible for them.

Appendix A

The analysis of the thermal conductivity signal is inherently complex due to the combined effects of the gas phase properties and the structural characteristics of the detection system (i.e., the Wheatstone bridge). The data analysis method developed to improve the interpretation of the reduction process leads to a crucial key point: establishing a robust correlation between the raw thermal conductivity signal and the extent of solid phase conversion in heterogeneous gas–solid reactions.

Significant slope variations within the signal indicate transitions between different reaction stages determined by the evolution of the predominant solid phase species and their respective kinetic and thermodynamic constraints. The response of the gas phase detector was quantitatively correlated with the overall degree of reduction of the solid sample. The data processing procedure in detail is: i) normalization to isolate gas conductivity changes; ii) signal complement to allow numerical integration; iii) cumulative integration using the trapezoidal rule; iv) the final processed curve. The presence of dead volume and axial dispersion effects in the early stages of the reaction led to deviations from the ideal behavior of the plug flow reactor. To correct the overestimation of hydrogen consumption due to these physical effects, the cumulative integral of the blank signal (i.e., in the absence of a solid sample) was subtracted from the experimental signal (cf., Fig. S12). The region enclosed between the two cumulative curves (cf., Fig. S12A) corresponds to the corrected aliquot of hydrogen consumed by the chemical reaction. Signal treatment performed through a sequence of these predefined mathematical steps rely exclusively on the physical characteristics of the TCD output and do not involve empirical corrections, filtering procedures, or arbitrary smoothing techniques. Owing to the intrinsic stability of the TCD response, problems typically associated with baseline drift or offset determination are inherently minimized, enhancing the robustness of the analysis. Baseline subtraction was temporally aligned with the experimental sequence (i.e., valve switching) to ensure accurate synchronization and to prevent artefacts arising from signal misalignment.

Appendix A. Supplementary data

Supplementary data to this article can be found online at https://doi.org/10.1016/j.cej.2026.176307.

Data availability

Data will be made available on request.

References

[1] S.J. Davis, et al., Net-zero emissions energy systems, Science 360 (6396) (1979), https://doi.org/10.1126/science.aas9793. Jun 2018.
[2] J.P. Birat, Society, materials, and the environment: the case of steel, Metals (Basel). 10 (3) (Mar. 2010), https://doi.org/10.3390/met10030331.
[3] S. Pauliuk, T. Wang, D.B. Müller, Steel all over the world: estimating in-use stocks of iron for 200 countries, Resour. Conserv. Recycl. 71 (Feb. 2013) 22–30, https://doi.org/10.1016/j.resconrec.2012.11.008.
[4] A. Chatterjee, Beyond the Blast Furnace, CRC Press, 2017, https://doi.org/10.1201/9781315138220.
[5] worldsteel association, 2024 World Steel in Figures, 2024. Accessed: Apr. 14, 2025. [Online]. Available, https://worldsteel.org/wp-content/uploads/World-Steel-in-Figures-2024.pdf.
[6] H.B. Lüngen, P. Schmöle, History, developments and processes of direct reduction of iron ores, Accessed: Jun. 17, 2025. [Online]. Available: chrome-extension://efaidnbmnnnibpcajpcglclefindmkaj, https://vdeh.de/media/luengen_dri_ecic_2022.pdf, 2022.
[7] I.F. Kurunov, The direct production of iron and alternatives to the blast furnace in iron metallurgy for the 21st century, Metallurgist 54 (5–6) (Sep. 2010) 335–342, https://doi.org/10.1007/s11015-010-9300-7.
[8] B. Anameric, S.K. Kawatra, Properties and features of direct reduced iron, Miner. Process. Extr. Metall. Rev. 28 (1) (Jan. 2007) 59–116, https://doi.org/10.1080/08827500600835576.
[9] M. Atsushi, H. Uemura, T. Sakaguchi, MIDREX process, Accessed: Nov. 23, 2023. [Online]. Available, https://www.kobelco.co.jp/english/ktr/pdf/ktr_29/050-057.pdf, 2010.
[10] M. Ahmed, M. Shahin, M. Elzeky, M. Ahmed, Effect of HYL process parameters on the quality of Iron ore reduction, J. Pet. Min. Eng. 18 (1) (Dec. 2016) 54–60, https://doi.org/10.21608/jpme.2016.37810.
[11] D. Nuber, E. Heinz, B. Rollinger, Circored fine ore direct reduction, Accessed: Jun. 17, 2025. [Online]. Available: https://www.academia.edu/1237578/Circored_fine_ore_direct_reduction, 2006.
[12] M.W. Erwee, P.C. Pistorius, Nitrogen in SL/RN direct reduced iron: origin and effect on nitrogen control in EAF steelmaking, Ironmak. Steelmak. 39 (5) (Jul. 2012) 336–341, https://doi.org/10.1179/1743281211Y.0000000076.
[13] P. Cavaliere, Direct Reduced Iron: Most Efficient Technologies for Greenhouse Emissions Abatement, in: Clean Ironmaking and Steelmaking Processes, Springer International Publishing, 2019, pp. 419–484, https://doi.org/10.1007/978-3-030-21209-4_8.
[14] V. Vogl, M. Åhman, L.J. Nilsson, Assessment of hydrogen direct reduction for fossil-free steelmaking, J. Clean. Prod. 203 (Dec. 2018) 736–745, https://doi.org/10.1016/j.jclepro.2018.08.279.
[15] D. Wagner, Etude expérimentale et modélisation de la réduction du minerai de fer par l'hydrogène, in: Ph.D. Thesis, Institut National Polytechnique de Lorraine, Nancy, France, 2008. Accessed: Jul. 01, 2024. [Online]. Available: https://tel.archives-ouvertes.fr/tel-00280689/.
[16] F. Patisson, O. Mirgaux, J.P. Birat, Hydrogen steelmaking. Part 1: Physical chemistry and process metallurgy, in: Mater. Tech. EDP Sciences, 2021, https://doi.org/10.1051/mattech/2021025.
[17] M. Åhman, et al., Hydrogen steelmaking for a low-carbon economy A joint LU-SEI working paper for the HYBRIT project [Online]. Available, www.sei.org, 2018.
[18] F. Cerciello, et al., Kinetics of iron reduction upon reduction/oxidation cycles, Int. J. Hydrog. Energy 65 (May 2024) 337–347, https://doi.org/10.1016/j.ijhydene.2024.04.008.
[19] W. Liu, J.Y. Lim, M.A. Saucedo, A.N. Hayhurst, S.A. Scott, J.S. Dennis, Kinetics of the reduction of wüstite by hydrogen and carbon monoxide for the chemical looping production of hydrogen, Chem. Eng. Sci. 120 (Dec. 2014) 149–166, https://doi.org/10.1016/j.ces.2014.08.010.
[20] C. Lan, Y. Hao, J. Shao, S. Zhang, R. Liu, Q. Lyu, Effect of H2 on blast furnace ironmaking: a review, Metals (Basel). 12 (11) (Nov. 2022) 1864, https://doi.org/10.3390/met12111864.
[21] F. Mauret, M. Baniasadi, H. Saxén, A. Feiterna, S. Hojda, Impact of hydrogenous gas injection on the blast furnace process: a numerical investigation, Metall. Mater. Trans. B 54 (4) (Aug. 2023) 2137–2158, https://doi.org/10.1007/s11663-023-02822-4.
[22] A.A. El-Geassy, Gaseous reduction of Fe2O3 compacts at 600 to 1050° C, J. Mater. Sci. 21 (11) (Nov. 1986) 3889–3900, https://doi.org/10.1007/BF02431626.
[23] Y. Zhai, L. Shao, C. Zhao, X. Zhang, H. Saxén, A numerical study of the thermochemical and aerodynamic states of H_2-intensive direct reduction shaft furnace, Steel Res. Int. (Nov. 2024), https://doi.org/10.1002/srin.202400567.
[24] D. Spreitzer, J. Schenk, Reduction of iron oxides with hydrogen—a review, Steel Res. Int. 90 (10) (Oct. 2019), https://doi.org/10.1002/srin.201900108.
[25] W.C. Malcolm, NIST JANAF Thermochemical Tables, 4th ed., American Chemical Society and the American Institute of Physics for the National Institute of Standards and Technology, 1998. Accessed: Apr. 15, 2025. [Online]. Available, https://janaf.nist.gov/pdf/JANAF-FourthEd-1998-1Vol1-Intro.pdf.
[26] W. Liu, J.Y. Lim, M.A. Saucedo, A.N. Hayhurst, S.A. Scott, J.S. Dennis, Kinetics of the reduction of wüstite by hydrogen and carbon monoxide for the chemical looping production of hydrogen, Chem. Eng. Sci. 120 (Dec. 2014) 149–166, https://doi.org/10.1016/j.ces.2014.08.010.
[27] F. Chen, Y. Mohassab, T. Jiang, H.Y. Sohn, Hydrogen reduction kinetics of hematite concentrate particles relevant to a novel flash ironmaking process, Metall. Mater. Trans. B Process Metall. Mater. Process. Sci. 46 (3) (Jun. 2015) 1133–1145, https://doi.org/10.1007/s11663-015-0332-z.
[28] K. He, Z. Zheng, Z. Chen, H. Chen, W. Hao, Kinetics of hydrogen reduction of Brazilian hematite in a micro-fluidized bed, Int. J. Hydrog. Energy 46 (5) (Jan. 2021) 4592–4605, https://doi.org/10.1016/j.ijhydene.2020.10.263.
[29] A.A. El-Geassy, M.I. Nasr, M.M. Hessien, Effect of reducing gas on the volume change during reduction of Iron oxide compacts, ISIJ Int. 36 (6) (1996) 640–649, https://doi.org/10.2355/isijinternational.36.640.
[30] M. Bahgat, M.H. Khedr, Reduction kinetics, magnetic behavior and morphological changes during reduction of magnetite single crystal, Mater. Sci. Eng. B Solid. State. Mater. Adv. Technol. 138 (3) (Apr. 2007) 251–258, https://doi.org/10.1016/j.mseb.2007.01.029.
[31] S. Hayashi, Y. Iguchi, K.O. Measured, Hydrogen reduction of liquid lron oxide fines in gas-conveyed systems, ISIJ Int. 34 (7) (1994) 555–561.
[32] A.A. Barde, J.F. Klausner, R. Mei, Solid state reaction kinetics of iron oxide reduction using hydrogen as a reducing agent, Int. J. Hydrog. Energy 41 (24) (Jun. 2016) 10103–10119, https://doi.org/10.1016/j.ijhydene.2015.12.129.
[33] Y.K. Rao, M. Moinpour, Kinetics of reduction of hematite with hydrogen gas at modest temperatures, Metall. Trans. B 14 (4) (Dec. 1983) 711–723, https://doi.org/10.1007/BF02653958.
[34] P. Heidebrecht, V. Galvita, K. Sundmacher, An alternative method for parameter identification from temperature programmed reduction (TPR) data, Chem. Eng. Sci. 63 (19) (Oct. 2008) 4776–4788, https://doi.org/10.1016/j.ces.2007.10.012.
[35] D. Spreitzer, J. Schenk, Iron ore reduction by hydrogen using a laboratory scale fluidized bed reactor: kinetic investigation—experimental setup and method for determination, Metall. Mater. Trans. B Process Metall. Mater. Process. Sci. 50 (5) (Oct. 2019) 2471–2484, https://doi.org/10.1007/s11663-019-01650-9.
[36] H. Wang, H.Y. Sohn, Hydrogen reduction kinetics of magnetite concentrate particles relevant to a novel flash ironmaking process, Metall. Mater. Trans. B Process Metall. Mater. Process. Sci. 44 (1) (Feb. 2013) 133–145, https://doi.org/10.1007/s11663-012-9754-z.
[37] E.T. Turkdogan, J.V. Vinters, Gaseous reduction of iron oxides: part III. Reduction-oxidation of porous and dense iron oxides and iron, Metall. Trans. A. 3 (6) (Jun. 1972) 1561–1574, https://doi.org/10.1007/BF02643047.
[38] E.T. Turkdogan, J.V. Vinters, Gaseous reduction of iron oxides: part I. Reduction of hematite in hydrogen, Metall. Trans. A. 2 (11) (Nov. 1971) 3175–3188, https://doi.org/10.1007/BF02814970.
[39] A. D'Angelo, E. Salucci, V. Russo, H. Grénman, H. Saxén, Hydrogen reduction of Iron oxide powder in thin layers, Ind. Eng. Chem. Res. 64 (1) (Jan. 2025) 158–170, https://doi.org/10.1021/acs.iecr.4c03138.

[40] A. D'Angelo, E. Salucci, V. Russo, H. Grenman, H. Saxén, Reduction kinetics of pure and industrial hematite samples with hydrogen in a small fixed bed system, Chem. Eng. J. (2025), https://doi.org/10.1016/j.cej.2025.165117.
[41] P. Cavaliere, A. Perrone, L. Dijon, A. Laska, D. Koszelow, Direct reduction of pellets through hydrogen: experimental and model behaviour, Int. J. Hydrog. Energy 49 (Jan. 2024) 1444–1460, https://doi.org/10.1016/j.ijhydene.2023.11.040.
[42] E. Salucci, A. D'Angelo, V. Russo, H. Grénman, H. Saxén, Review on the reduction kinetics of Iron oxides with hydrogen-Rich gas: experimental investigation and modeling approaches, Ind. Eng. Chem. Res. 64 (1) (Jan. 2025) 1–35, https://doi.org/10.1021/acs.iecr.4c03136.
[43] E. Salucci, A. D'Angelo, V. Russo, H. Grénman, H. Saxén, Kinetic modeling and parameter estimation of thin-layer iron oxide reduction with hydrogen in a fixed-bed reactor, Chem. Eng. J. 529 (Feb. 2026) 172848, https://doi.org/10.1016/j.cej.2026.172848.
[44] E. Salucci, A. D'Angelo, V. Russo, H. Grénman, H. Saxén, Modelling of iron oxide reduction with hydrogen in a small fixed bed, Chem. Eng. Sci. 292 (Jun. 2024) 119934, https://doi.org/10.1016/j.ces.2024.119934.
[45] T. Melchiori, Study of Non Catalytic Gas-Solid Reactions: Development of a Single Particle Model, in: Doctoral Thesis, Università degli studi di Padova, Padova, 2014. Accessed: Jul. 02, 2024. [Online]. Available, https://hdl.handle.net/11577/3423565.
[46] M.S. Valipour, Mathematical modeling of a non-catalytic gas-solid reaction: hematite pellet reduction with syngas, Trans. C: Chem. Chem.l Eng. 16 (2) (2009). Accessed: Aug. 11, 2025. [Online]. Available, https://scientiairanica.sharif.edu/article_3274_6b27e78d914ba8e032c3a58da5168cf5.pdf.
[47] Chemstations, CHEMCAD v. 7.0, Accessed: Apr. 23, 2025. [Online]. Available, http://www.chemstations.com/, 2020.
[48] M. Bahgat, M.H. Khedr, Reduction kinetics, magnetic behavior and morphological changes during reduction of magnetite single crystal, Mater. Sci. Eng. B Solid. State. Mater. Adv. Technol. 138 (3) (Apr. 2007) 251–258, https://doi.org/10.1016/j.mseb.2007.01.029.
[49] L.Y. Xing, Z.S. Zou, Y.X. Qu, L. Shao, J.Q. Zou, Gas–solid reduction behavior of in-flight fine hematite ore particles by hydrogen, Steel Res. Int. 90 (1) (Jan. 2019), https://doi.org/10.1002/srin.201800311.
[50] A.A. El-Geassy, V. Rajakumar, Influence of particle size on the gaseous reduction of wustite at 900-1100.DEG.C, Trans. Iron Steel Inst. Japan 25 (12) (1985) 1202–1211, https://doi.org/10.2355/isijinternational1966.25.1202.
[51] A.A. El-Geassy, Gaseous reduction of Fe2O3 compacts at 600 to 1050° C, J. Mater. Sci. 21 (11) (Nov. 1986) 3889–3900, https://doi.org/10.1007/BF02431626.
[52] L. Shao, Q. Wang, Y. Qu, H. Saxén, Z. Zou, A numerical study on the operation of the H_2 shaft furnace with top gas recycling, Metall. Mater. Trans. B Process Metall. Mater. Process. Sci. 52 (1) (Feb. 2021) 451–459, https://doi.org/10.1007/s11663-020-02020-6.